



HAL
open science

Geodetic Observations of Shallow Creep on the Laohushan-Haiyuan Fault, Northeastern Tibet

Yanchuan Li, Jean-Mathieu Nocquet, Xinjian Shan, Xiaogang Song

► **To cite this version:**

Yanchuan Li, Jean-Mathieu Nocquet, Xinjian Shan, Xiaogang Song. Geodetic Observations of Shallow Creep on the Laohushan-Haiyuan Fault, Northeastern Tibet. *Journal of Geophysical Research : Solid Earth*, 2021, 126 (6), pp.e2020JB021576. 10.1029/2020JB021576 . hal-03578631

HAL Id: hal-03578631

<https://hal.science/hal-03578631>

Submitted on 12 Aug 2022

HAL is a multi-disciplinary open access archive for the deposit and dissemination of scientific research documents, whether they are published or not. The documents may come from teaching and research institutions in France or abroad, or from public or private research centers.

L'archive ouverte pluridisciplinaire **HAL**, est destinée au dépôt et à la diffusion de documents scientifiques de niveau recherche, publiés ou non, émanant des établissements d'enseignement et de recherche français ou étrangers, des laboratoires publics ou privés.

Copyright

JGR Solid Earth

RESEARCH ARTICLE

10.1029/2020JB021576

Special Section:

100-year Anniversary of the Great 1920 Haiyuan Earthquake: What have We Learnt on Large Continental Earthquakes and Faults?

Key Points:

- Of three creep segments on the Laohushan-Haiyuan fault, two are located along fault sections that ruptured during the 1920 M~8 earthquake
- Vertical motion leads to overestimation of the creep rate on the Laohushan fault; our refined creep rate is 2.5 ± 0.4 mm/a
- Our findings support that large earthquakes can rupture pre-existing creep regions or that they can generate long-lasting afterslip or creep

Supporting Information:

Supporting Information may be found in the online version of this article.

Correspondence to:

Y. Li and X. Shan,
yanchuan@ies.ac.cn;
xjshan@ies.ac.cn

Citation:




Li, Y., Nocquet, J.-M., Shan, X., & Song, X. (2021). Geodetic observations of shallow creep on the Laohushan-Haiyuan fault, northeastern Tibet. *Journal of Geophysical Research: Solid Earth*, 126, e2020JB021576. <https://doi.org/10.1029/2020JB021576>

Received 21 DEC 2020

Accepted 5 JUN 2021

© 2021. American Geophysical Union.
 All Rights Reserved.

Geodetic Observations of Shallow Creep on the Laohushan-Haiyuan Fault, Northeastern Tibet

Yanchuan Li^{1,2} , Jean-Mathieu Nocquet^{2,3} , Xinjian Shan¹ , and Xiaogang Song¹

¹State Key Laboratory of Earthquake Dynamics, Institute of Geology, China Earthquake Administration, Beijing, China,

²Université Côte d'Azur, Geoazur, IRD, CNRS, Observatoire de la Côte d'Azur, Valbonne, France, ³Université de Paris, Institut de Physique du Globe de Paris, Paris, France

Abstract We investigated the spatial distribution of aseismic creep on the Laohushan-Haiyuan fault using Global Positioning System (GPS) data (1999–2017) and Interferometric Synthetic Aperture Radar (InSAR) data (2003–2010). Comparisons among GPS, InSAR line-of-sight (LOS) rates, and leveling show that neither leveling nor GPS vertical velocities can fit the vertical signal mapped into the LOS, implying either complicated vertical crustal deformation in northeastern Tibet and/or complex error structures in the InSAR data. Thus, we combined horizontal GPS with high-pass filtered InSAR data to produce a continuous LOS rate map crossing the fault. Our geodetic data reveal three creep sections along the fault. Both the restored LOS data and decomposed ascending and descending InSAR data highlight the fact that vertical motion can cause an overestimation of creep rate; we obtained a refined creep rate of 2.5 ± 0.4 mm/a on the Laohushan fault. We further identified a 10 km-long, $\sim 3\text{--}5$ mm/a creep section ($\sim 104.2^\circ\text{E}\text{--}104.3^\circ\text{E}$) and a 43 km-long, $\sim 1\text{--}3$ mm/a creep section ($\sim 105.3^\circ\text{E}\text{--}105.7^\circ\text{E}$) on the western and eastern Haiyuan fault respectively. Both are located on fault sections that ruptured during the 1920 M~8 earthquake, suggesting that the 1920 earthquake was able to cross pre-existing creep sections or that the fault shows heterogeneous relocking after large earthquakes, with creep lasting decades on some parts of the rupture. Fault coupling shows a highly variable rate of slip deficit accumulation along strike, suggesting that coupling might significantly evolve during the period between two large earthquakes.

Plain Language Summary Ample observations document slip on a fault plane is seismic and/or aseismic; the former situation refers to a fault slips suddenly and produce earthquakes, the latter means a fault slips gradually without generating seismic energy. Studying the fault-creep activity contributes to better understand the seismic behavior of crustal faults. We focus on the Haiyuan fault system, which is located on the northeastern margin of Tibet. Several large earthquakes occurred along the fault system in the past, including the 1920 M~8.0 Haiyuan and the 1927 M~8.3 Gulang earthquakes. Using Interferometric Synthetic Aperture Radar (InSAR) and Global Positioning System (GPS) data, we identified three creep sections along the fault. Our results show vertical deformation that has mapped into the InSAR line-of-sight (LOS) could leads to overestimation of the creep rate. Besides, our findings imply either large earthquakes can rupture creep regions or they can generate long-lasting afterslip/creep.

1. Introduction

In simple models, faults are considered to be locked over the entire seismogenic zone during the interseismic phase and slip only during earthquakes (e.g., Reid, 1910). However, over the last decades, high spatial resolution observations have shown that some continental faults exhibit dual mechanical behavior, where locked segments coexist with sections where steady slip (or creep) occurs aseismically within the seismogenic zone of the fault. Creeping segments along faults are thought to limit the ability of the fault to generate major earthquakes (e.g., Avouac, 2015). Indeed, when the rate of aseismic creep is equal to or larger than the relative motion of surrounding blocks, little or no elastic strain accumulates on the fault. An example of this behavior is the north coast section of the San Andreas Fault (e.g., Lienkaemper et al., 2014). In contrast, when the fault segment slips at a creep rate lower than the tectonic loading rate, a slip deficit still accumulates. In this case, earthquakes can still occur, such as those along the North Anatolian Fault (NAF; e.g., Çakir et al., 2005). Furthermore, aseismic creep can be the triggering factor for small to moderate-size earthquakes, such as the creep-driven M_1 4.6–4.7 earthquakes on the Laohushan fault between 2006

and 2007 (Jolivet et al., 2013). Aseismic creep, on the other hand, can impede/arrest the propagation of an earthquake rupture (e.g., Avouac, 2015). Thus, identifying and quantifying the spatial distribution, rates, and depths of aseismic slip constitute an important aspect in characterizing potential rupture scenarios of future earthquakes (e.g., Bürgmann et al., 2000; Li, Shan, et al., 2018).

The Haiyuan fault system is a major continental left-lateral strike-slip fault in northeastern Tibet that accommodates the eastward motion of Tibet (Figure 1). It consists of the Lenglongling, Jinqianghe, Mao-maoshan, Laohushan, and Haiyuan faults. The Haiyuan fault is further segmented into western (HYW), middle (HYM), and eastern (HYE) segments; this fault hosted the 1920 $M \sim 8.0$ earthquake, which generated ~ 240 km of surface rupture, with a maximum slip of ~ 10 m at its center (Q. Deng et al., 1986). Faults from Lenglongling to Laohushan constitute the Tianzhu seismic gap, in which no $M 7+$ earthquakes have been recorded over the past few centuries despite clear geomorphic evidence for coseismic fault rupture (Gaudeamer et al., 1995).

Global Positioning System (GPS) and Interferometric Synthetic Aperture Radar (InSAR) have been extensively used to quantify interseismic deformation along the Haiyuan fault system. Depending on the data used and the inversion model, slip rates of between 5 and 10 mm/a have been estimated (e.g., Cavalié et al., 2008; Daout et al., 2016; Gan et al., 2007; Jolivet et al., 2012, 2013; Li, Liu et al., 2018; Li et al., 2016, 2017). Recent studies highlight along strike changes in locking depth (from 2 to 22 km; Li et al., 2017), with a 35 km-long section that creeps aseismically at ~ 5 mm/a, a rate of full tectonic loading, at the eastern end of the Laohushan fault (Jolivet et al., 2012).

However, despite numerous studies, aseismic slip behavior along the Haiyuan fault system has not yet been systematically quantified. Based on GPS data, Li et al. (2017) proposed fault locking from the Lenglongling fault to the Liupanshan fault, but the study suffered from low spatial resolution close to the fault, preventing any existing creep signals from being identified. InSAR data provide a way to constrain interseismic fault coupling (ISC) with dense near fault observations. However, a limiting factor of InSAR is that an interferogram only measures one component of the surface deformation. An open question in using InSAR is how best to evaluate and separate vertical deformation that has mapped into the line-of-sight (LOS). Previous studies have assumed that InSAR LOS displacements are fault-parallel and horizontal (Cavalié et al., 2008; Jolivet et al., 2012, 2013; Song et al., 2019). Such an assumption is challenged by leveling measurements (1970–2012) that report ~ 1 – 2 mm/a uplift motion across the Haiyuan fault system (Figure 2) in spite of a low spatial resolution for the leveling profiles (Hao et al., 2014). For the descending Environmental Satellite (Envisat; incidence angle of 23° and azimuth of 193°) adopted by previous studies, the LOS displacement vector is $d_{\text{LOS}} = [d_N, d_E, d_V] \cdot [-0.094, 0.391, 0.916]^T$, meaning that LOS displacement is at least twice as sensitive to vertical deformation as it is to horizontal deformation. Considering the non-negligible vertical crustal deformation in northeastern Tibet, it is crucial to evaluate potential vertical deformation and carefully separate them in InSAR LOS maps, so that the LOS maps can contribute to improve the ISC along the fault system. Furthermore, these LOS maps are essential for exploring if multiple sections of the Haiyuan fault system are creeping, as observed along the NAF (e.g., Bilham et al., 2016) and Hayward Fault (e.g., Chaus-sard et al., 2015).

Creep along the Laohushan fault also provides a topic for further study. Considering potential vertical deformation in LOS displacements, a re-evaluation of the creep rate is necessary, with implications for both seismic potential and insight into creep behavior. Moreover, the physical mechanism of the shallow creep is poorly understood. Jolivet et al. (2013) reported that the creep rate scales logarithmically with the friction coefficient, implying a rate strengthening regime. Chen et al. (2018) proposed that the creep is either the afterslip following the moderate 2000 Mw 5.5 Jingtai earthquake (Figure 1) or in response to the great 1920 $M \sim 8$ Haiyuan earthquake.

In this study, we used geodetic data composed of new/dense GPS (1999–2017), leveling (1970–2012; Hao et al., 2014), and Envisat SAR (2003–2010; Song et al., 2019) from six descending tracks and one ascending track across the Laohushan-Haiyuan fault to study aseismic slip behavior. We compared the different datasets to investigate if vertical deformation contributes to the InSAR LOS, and combined GPS horizontal velocities with InSAR descending displacements to investigate any creep sections along the fault and to recover robust creep rates. Elastic block modeling of the combined geodetic data provides a spatially

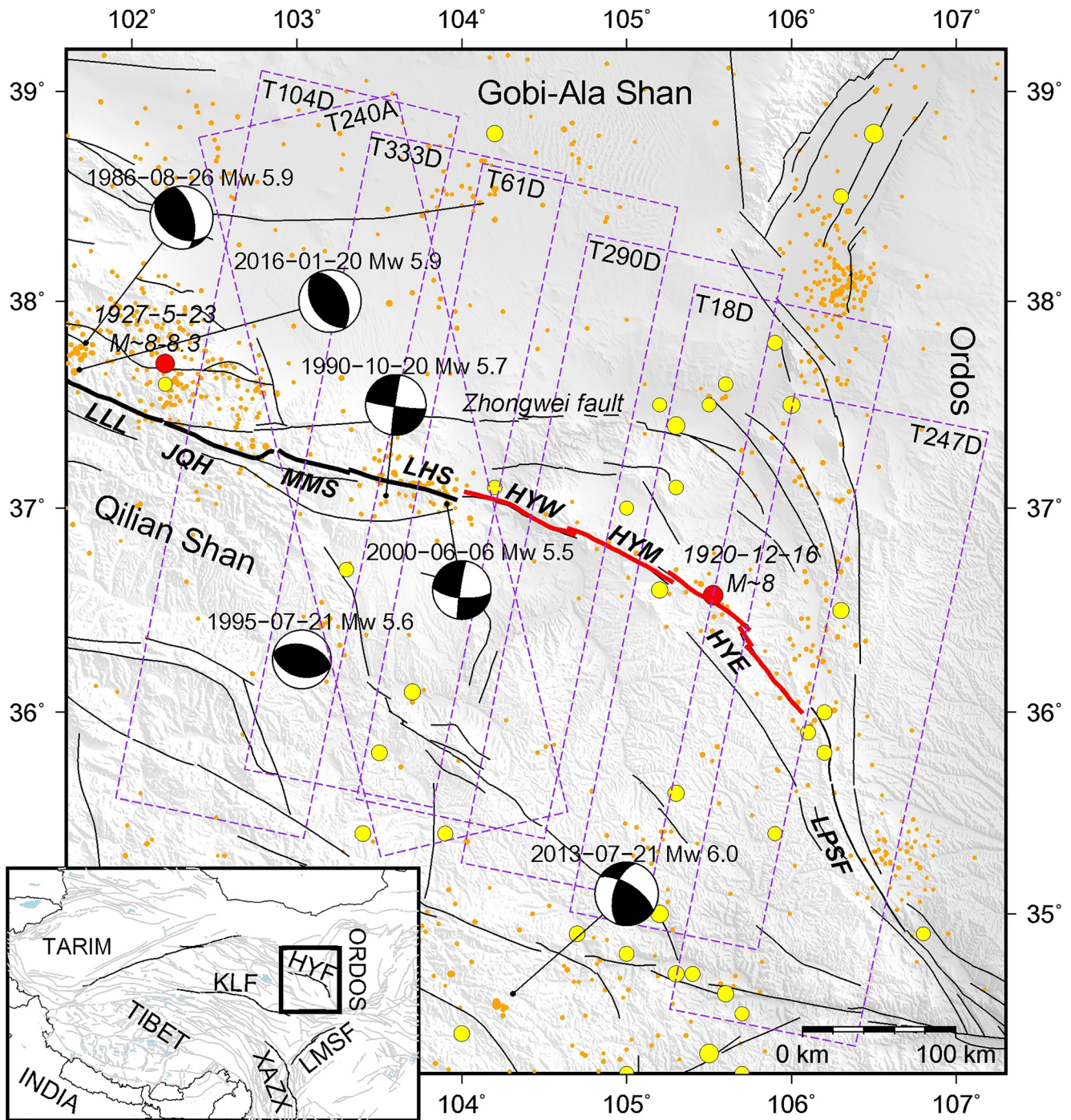


Figure 1. Regional tectonic map of the northeastern Tibetan Plateau. Bold red lines correspond to surface ruptures during the 1920 M~8 Haiyuan earthquake (Q. Deng et al., 1986). Bold black lines represent the Tianzhu seismic gap (Gaudemer et al., 1995). Thin black lines indicate regional faults. Orange dots represent earthquakes from 1970 to 2017 from the China Earthquake Administration (<http://data.earthquake.cn/>). Yellow circles correspond to earthquakes with magnitudes equal to or greater than 6.0 between 780 BCE and 1969 CE (<http://data.earthquake.cn/>). The two red circles show the epicenters of the 1920 Haiyuan and 1927 Gulang earthquakes (<http://data.earthquake.cn/>). Focal mechanism solutions ($M_w \geq 5.5$, 1976–2018) come from the Global Centroid Moment Tensor (GCMT). Dotted rectangles show the coverage of Interferometric Synthetic Aperture Radar (InSAR) tracks used in this study. The inset map shows the study area. LLL: Lenglongling fault, JQH: Jinqianghe fault, MMS: Maomaoshan fault, LHS: Laohushan fault, HYW: Western Haiyuan segment, HYM: Middle Haiyuan segment, HYE: Eastern Haiyuan segment, LPSF: Liupanshan fault; ATF: Altyn Tagh fault; KLF: Kunlun fault; XAZX: Xianshuihe-Anninghe-Zemuhe-Xiaojiang fault system; LMSF: Longmenshan fault.

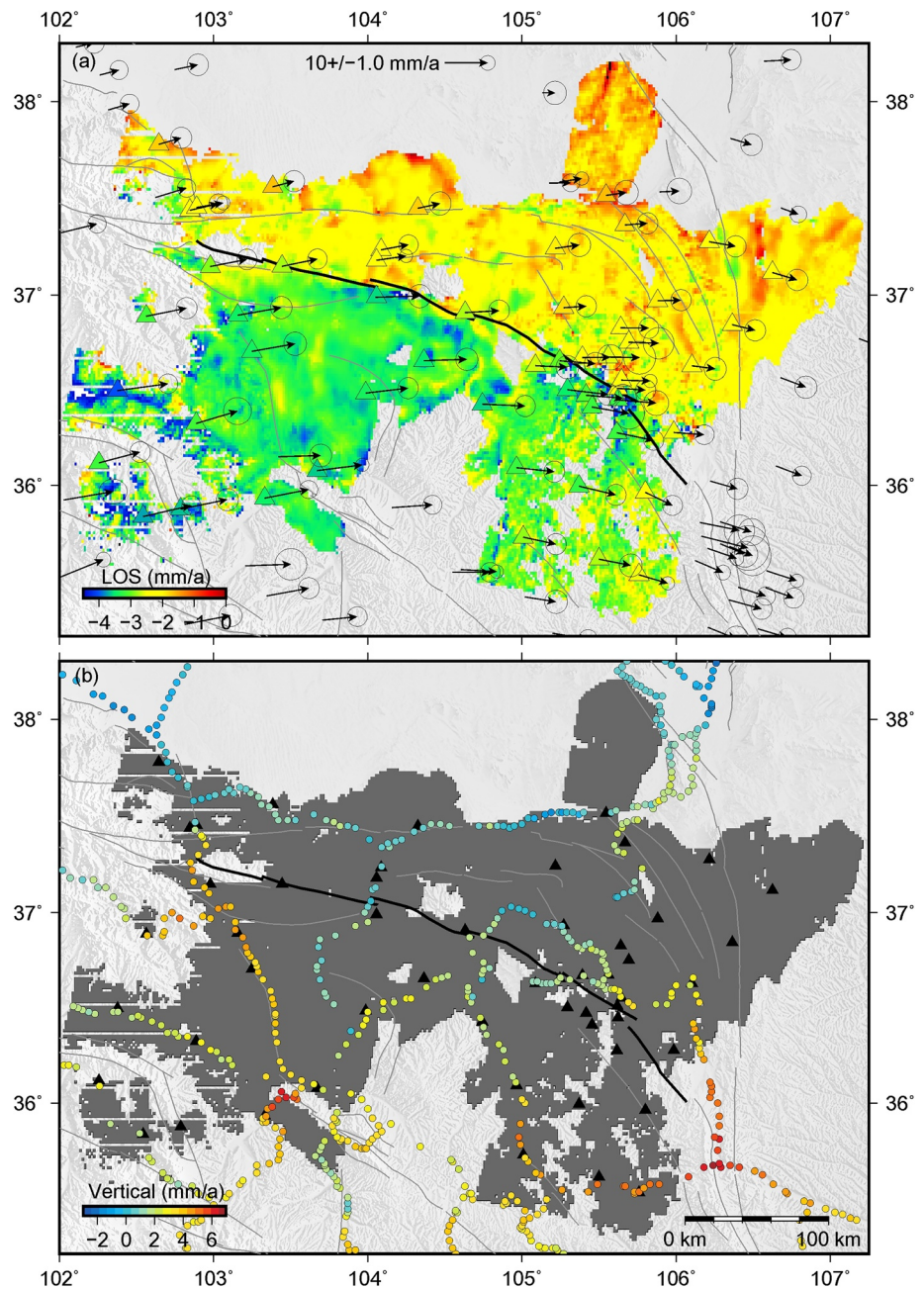


Figure 2. Restored line-of-sight (LOS) displacements, Global Positioning System (GPS), and leveling velocity field of northeastern Tibet. (a) Bold black lines show the Haiyuan fault system. GPS velocities are with respect to the stable Eurasian plate, with error ellipses indicating the 95% confidence level. The colors of triangles represent LOS projections of horizontal GPS velocities. (b) The colors of circles donate the vertical velocities of leveling sites. The gray shaded area indices the coverage of InSAR, with black triangles representing GPS sites located within the area.

variable fault coupling map. Geodetic and seismic observations, fault coupling, and historical earthquake ruptures were integrated to infer the potential mechanisms of shallow creep and seismic hazard along the Laohushan-Haiyuan fault. Decomposing of descending and ascending tracks across the Laohushan fault provides new insight into its creep behavior.

2. Geodetic Data

2.1. GPS Data and Processing

We obtained GPS data from two sources: the majority were from the Crustal Movement Observation Network of China (CMONOC I/II), including 24 continuous stations from 2010 to 2017 (two of which started to operate from 1999) and 164 campaign-mode stations conducted during 5–10 campaigns in 1999–2017. In addition, we collected data from 14 newly built campaign-mode stations across the Haiyuan fault (Figure S1). These sites were installed in 2013 and were measured annually from 2013 to 2017. We used Trimble NetR9 and Topcon NetG5 receivers with choke ring antennas to perform continuous observations for at least 72 h per site during each campaign.

The GAMIT/GLOBK 10.6 software (Herring et al., 2016) was used to process the GPS data. Raw pseudo-range and phase observations were first processed together with 20 International GNSS Service (IGS) stations, which are distributed around mainland China, to obtain daily loosely constrained station coordinates and satellite orbit parameters. We employed IGS precise orbits and Earth orientation parameters, absolute antenna phase center calibrations, and the Finite Element Solution (FES) 2004 ocean tide-loading model during daily data processing. The position time series of each site was carefully inspected to detect and remove outliers by using the GPS time series analysis software, PYACS (Nocquet, 2017). Then, the daily solutions were transformed into the International Terrestrial Reference Frame 2014 (ITRF 2014) by estimating seven transformation parameters (including orientation, translation, and scale) using the 20 IGS stations. Finally, the GPS site velocities were transformed into a Eurasia-fixed reference frame using the Euler vector for Eurasia (Altamimi et al., 2017; Figure 2 and S1). Since most of the GPS sites were measured in campaign-mode, we did not estimate GPS vertical velocities in the data processing. The least squares fitting results indicate an average velocity uncertainty of 0.4 mm/a. To avoid underestimation, we reweighted sites velocity uncertainties by multiplying the standard deviations with a scale factor between the average uncertainty in Kreemer et al. (2014) and ours. The factors were 2.6 and 2.5 for the east and north components, respectively, leading to uncertainties of ~ 1.0 mm/a (1σ).

During the GPS data span (1999–2017), several destructive earthquakes occurred in and around mainland China, including the 2001 Mw 7.8 Kokoxili earthquake, the 2008 Mw 7.9 Wenchuan earthquake, and the 2011 Mw 9.0 Tohoku (Japan) earthquake. Among them, the Wenchuan and Tohoku earthquakes produced obvious coseismic deformation in northeastern Tibet. Therefore, we added offset parameters to the GPS position time series to correct for those coseismic deformations. Our study region is more than 500 km away from the epicenter of the Wenchuan earthquake, which generated postseismic displacements within a ~ 200 km area around the surface ruptures (e.g., Diao et al., 2018). Therefore, we did not consider the postseismic transients of the Wenchuan earthquake in our GPS data processing. Our GPS velocity solution has been uploaded for open access (<https://osf.io/8b72w/>).

2.2. InSAR Data

The Envisat SAR data, including six tracks of descending images (across the Laohushan-Haiyuan fault) and one track of ascending images (across the Laohushan fault) spanning 2003 to 2010, were adopted from Song et al. (2019). The ROI_PAC software (Rosen et al., 2004) was used to compute interferograms. In data processing, atmospheric corrections are crucial for retrieving small ground displacements of a few millimeters per year. Tropospheric delays can be considered as the sum of a contribution of turbulent delays and a contribution from delay in a stratified troposphere. Turbulent delays are mostly spatially random and uncorrelated from one acquisition to the next; thus, they were efficiently removed by stacking independent interferograms. For the latter, Song et al. (2019) used atmospheric data from the European Center for Medium-Range Weather Forecasts (ECMWF) to simulate and correct for the those delays. Subsequently, a ramp simulating any orbital linear residues was fitted and removed for each interferogram. Finally, stacking all interferograms allowed us to infer the average LOS rate map.

The InSAR LOS rate map (Figure S2) of Song et al. (2019) includes contributions from horizontal and vertical deformation, and non-tectonic spatially correlated noise. Here, we focused on tectonic deformation. Based on the data of Song et al. (2019), we first masked InSAR data located in regions with obvious

subsidence, such as those related to groundwater extraction or coal mining. The six descending images were used to evaluate the consistency between different geodetic datasets, and subsequent elastic block modeling (see Section 4.2). The ascending image was further analyzed with one descending image (see Section 6.2); a simple decomposition of LOS into horizontal and vertical velocities highlights non-negligible vertical deformation across the Laohushan fault. Hereafter, unless otherwise specified, InSAR refers to descending images.

2.3. Leveling Data

We took the leveling velocity solution from Hao et al. (2014). The leveling benchmarks were measured across northeastern–eastern Tibet according to first-order leveling standards, and a total of two to seven campaigns were conducted during the period of 1970–2012. The linear rate (adjustment) was expressed in a regional reference frame, which was realized by nine GPS stations distributed over the region and with occupations spanning 1998–2008. We show the leveling vertical velocity solution for northeastern Tibet in Figure 2 and S3.

3. Geodetic Data Comparison and Combination

3.1. Methodology

We evaluated the consistency between GPS (hereafter, unless otherwise specified, GPS refers to horizontal GPS velocity), leveling, and InSAR LOS rate maps. Three different comparisons were made.

1. InSAR versus GPS + leveling. The leveling solution allowed us to add a vertical component to the horizontal GPS velocity. In practice, we first selected leveling sites located in a 5-km radius from the GPS stations, and took the leveling velocity to simulate the vertical motion of the GPS site. Then, we projected the 3D velocity onto InSAR LOS according to local incidence angles at each GPS site. The InSAR data, which are located within a 1-km radius around the GPS sites, were averaged and used for comparison with the GPS + leveling projection.
2. InSAR versus independent 3D GPS. Since we did not estimate the GPS vertical velocities in our data processing, we instead used the 3D GPS velocity solution (Figure S4) from Liang et al. (2013) to test this approach. We used only GPS sites having both horizontal and vertical velocities in subsequent comparisons. Similar to above, we first projected the 3D GPS velocities onto the InSAR LOS using local incidence angles, and then compared it with the observed InSAR LOS values.
3. Filter method to combine InSAR with GPS. We used the remove-filter-restore method proposed by Wei et al. (2010). The principle of this method is to combine the long wavelength displacements of GPS with short wavelength displacements of InSAR, and produce a LOS rate map that is not contaminated by long wavelength-correlated noise, such as orbital residuals. The method ensures that InSAR velocities agree with GPS at the longest wavelengths, while still preserving short-wavelength features (e.g., creep signals) that make InSAR contributions valuable in the near field of the fault. Here, we aimed at combining horizontal GPS velocity with InSAR. First, we used the GMT *gpsgridded* module (Sandwell & Wessel, 2016) to interpolate 2D GPS velocities, and projected the interpolated velocities onto LOS. The interpolation-derived LOS map was then removed from the observed InSAR data. LOS residuals were then high-pass filtered with a cutoff wavelength of 50 km, which was determined using the average spacing of GPS sites. Finally, the filtered LOS residuals were added back to the interpolation-derived LOS map. The final restored LOS velocity map is expressed in the same reference frame as GPS (Figure 2). The filter approach removes not only bias but also potential long-wavelength vertical rates in the observed InSAR LOS rate map. Nevertheless, small scale vertical deformation might still be present in the restored InSAR LOS rate map, and its effect on estimating creep rate along the Laohushan-Haiyuan fault is discussed in Section 6.1.

3.2. Comparison Results

The results (Figure 3) show that the LOS projection of horizontal GPS velocities (blue dots) deviate systematically from observed InSAR values, with a Root Mean Square (RMS) of 1.9 mm/a. This indicates either

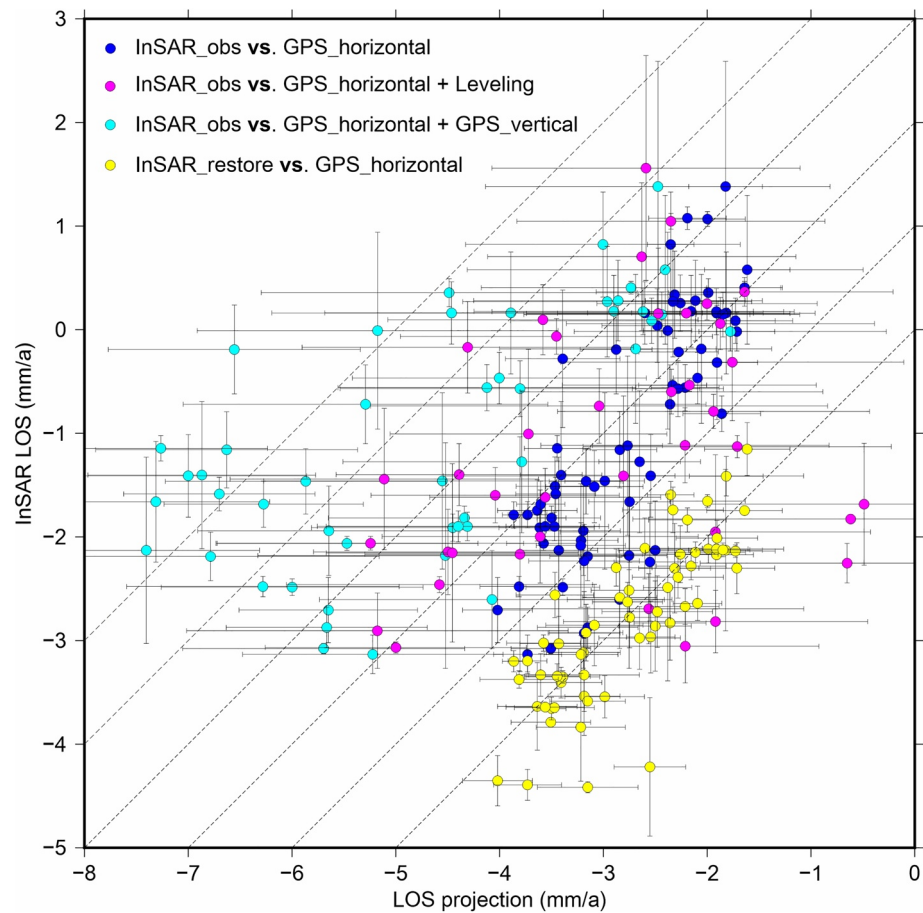


Figure 3. Comparison of different geodetic datasets. Blue dots show the observed Interferometric Synthetic Aperture Radar (InSAR) line-of-sight (LOS) values (y axis) versus the observed Global Positioning System (GPS) horizontal velocities projected to LOS (x axis). Magenta dots represent the observed InSAR LOS values (y axis) versus “GPS horizontal + leveling vertical” projected to LOS (x axis). Cyan dots represent the observed InSAR LOS values (y axis) versus “GPS horizontal + GPS vertical” (Liang et al., 2013) projected to LOS (x axis). Yellow dots represent the restored InSAR LOS values (y axis) versus the observed GPS horizontal velocities projected to LOS (x axis). Error bars represent 1σ uncertainties. Dotted lines show the 1:1 relationships.

vertical deformation, systematic orbital residuals, or a combination of both in the observed InSAR LOS displacements; the former is most likely the dominant factor. Figure 3 shows that using the leveling-derived vertical velocity to simulate vertical motion of GPS sites leads to higher dispersion in the LOS direction (magenta dots), with RMS increasing to 3.9 mm/a. The inconsistency can be attributed to several factors, including systematic orbital residuals in InSAR, temporal variations in vertical rates over the past few decades (because of GPS, leveling, and InSAR data spanning different periods), systematic errors in leveling, or some combination of the above. A similar disagreement between the 3D GPS and InSAR is observed (cyan dots), with an RMS value of 2.3 mm/a. The increase in scattering suggests that this originates in highly scattered GPS vertical rates.

Compared with results that adopt external datasets, the filter method ensures that horizontal GPS and restored InSAR (yellow dots) are consistent at the 0.5 mm/a level (RMS; Figure 3). Although not perfect, the restored InSAR data allowed the database to investigate aseismic slip along the Laohushan-Haiyuan fault, and were hence used in the modeling. The above comparison results indicate either complicated vertical crustal deformation in northeastern Tibet and/or complex error structures in InSAR, highlighting the significance of accounting for vertical deformation in the observed InSAR LOS map.

4. Modeling Strategy

4.1. Deriving Creep Rate From Cross-Fault Profile Velocities

We used the restored LOS data to investigate surface creep along the Laohushan-Haiyuan fault. The creep rate is defined as the fault-parallel velocity offset across the fault. Before modeling cross-fault profile velocities, we first analyzed GPS velocity results along five profiles perpendicular to the fault (Figure S1). Profiles were roughly selected according to the fault segmentation. The results show a strike-slip rate of 5.4 ± 1.1 mm/a (LLL) decreasing eastward to 2.7 ± 1.2 mm/a (HYE), and shortening rate of ~ 0 –0.5 mm/a across the Laohushan-Haiyuan fault (Figures S5 and S6). These results imply strike-slip dominated motion of the fault. Text S1 and S2 in the supporting information detail the modeling strategy and analysis. Since the restored LOS map is expressed in the same reference frame as GPS, north components contribute less than 0.15 mm/a to LOS; therefore the restored InSAR data are assumed to be purely related to fault-parallel motion.

In cross-fault profile velocity modeling, LOS velocities were taken in small boxes crossing the fault (2 km normal to the fault and 2 km along strike). To evaluate the impact of low signal-to-noise ratios in LOS data, we tested multiple choices of profile length on either side of the fault to estimate the creep rate (i.e., 1–5 km normal to the fault), and varied the mask width from 0.1 to 1 km (i.e., we explored how much data to mask out near the fault; Figure S7). Text S3 presents more details and analysis of this process. Results of all profile choices show similar overall along-strike patterns. In our preferred scheme, the profiles extend for 2 km on either side of the fault and pixels within 0.1 km of the fault trace are masked out, which keeps a balance between the signal-to-noise ratio and creep rate estimation bias. For each profile, we performed a linear regression to fit a straight line on each side of the fault, and the creep rate was estimated by differencing the modeled fault-parallel velocities ($x = \pm 0.1$ km) across the fault. Figure 4 shows examples of creep rate estimation for profiles crossing both the creep and locked segments.

4.2. Elastic Block Model

Surface creep results provide information on aseismic slip at shallow depths, while fault coupling provides information of strain accumulation average over depth. We used an elastic block model, which we implemented using the TDEFNODE package (McCaffrey, 2009), to invert for the spatial distribution of interseismic coupling along the Laohushan-Haiyuan fault. This method assumes that the observed geodetic data (GPS and restored InSAR) is the result of block rotation, strain rate within blocks, and elastic deformation induced by locking patches along the fault plane. In the model, interseismic backslip is applied along faults to solve for the fault coupling coefficient, a unitless parameter between 0 (fully creeping) and 1 (fully locked).

We adopted four elastic blocks in the model (Figure S8), and set the vertical geometry for the Laohushan-Haiyuan fault (patch size of 5 km along strike and 1 km along dip). We did not adopt smoothing factors in the model to avoid smoothed results that might obscure creep signals. Weights for GPS and InSAR data were set to be equal. Since this model is a further improvement of our previous one, we refer the reader to our previous study for detailed block modeling information (Li et al., 2017).

To check the robustness of our estimates of fault coupling, we calculated the sensitivity of the model to the geodetic data set, which is based on the model resolution matrix and defined as $S = G^t (GG^t)^{-1} G$, where G is the matrix of the elastic Green's function used in the interseismic backslip calculation. Every row in S corresponds to a model parameter and the value varies from one in well-resolved areas to 0 in unresolved areas. The result shows that the available GPS data well constrain (resolution ≥ 0.6) the upper 10–15 km of the HYE, while resolution is more limited along other segments (Figure S9). Adding InSAR data resulted in good resolution above depths of ~ 10 –15 km along the Laohushan-Haiyuan fault.

We also ran a forward model (along-strike/along-dip patch sizes of 10×10 km) with starting coupling values of either 1 or 0, and then added random errors with the same variance as those of the GPS and InSAR to the forward velocities. Finally, we inverted the fault coupling along the Laohushan-Haiyuan fault. Consistent with the above resolution test, checkerboard result shows that lateral variations of 10 km are

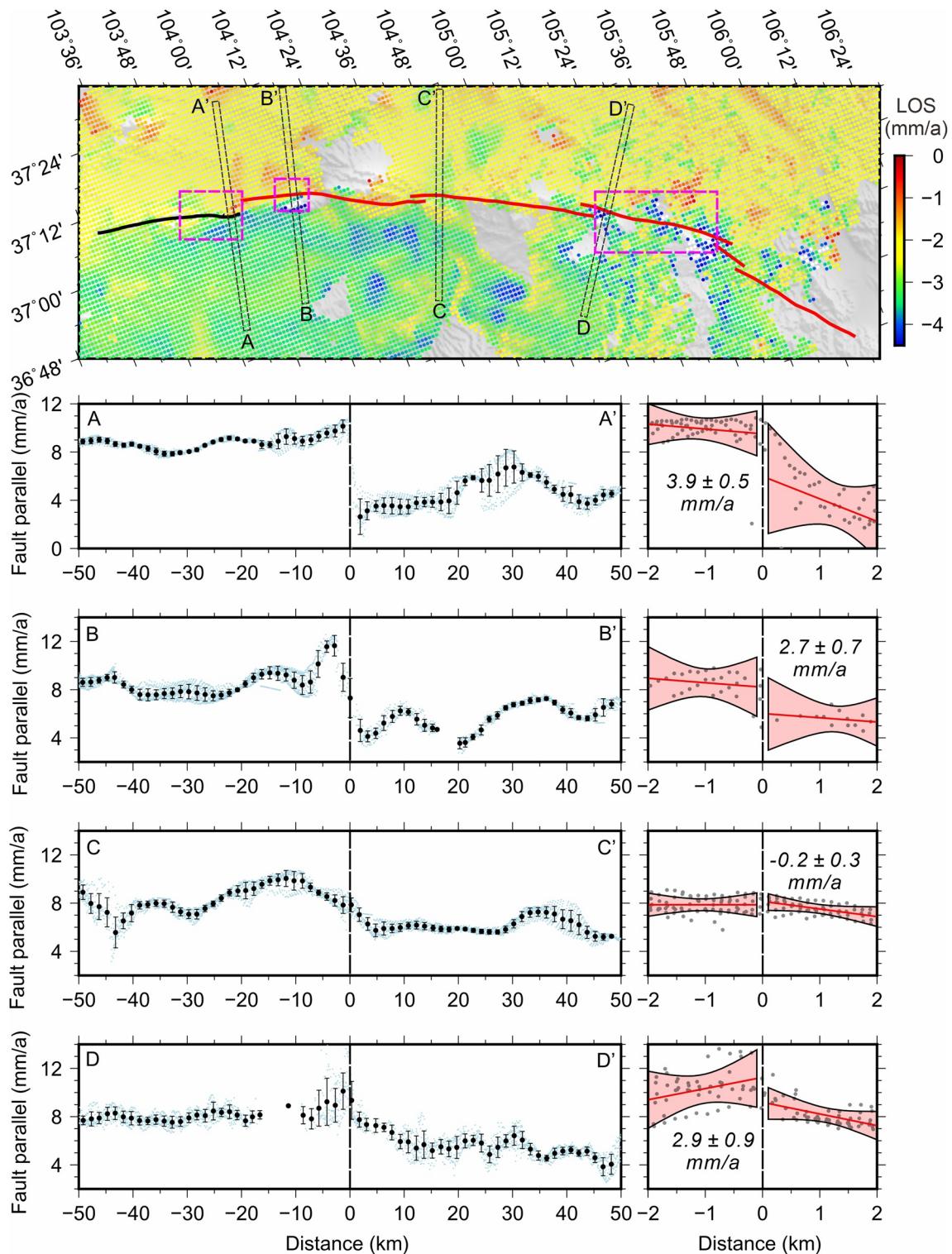


Figure 4. Map of the restored line-of-sight (LOS) displacements across the Laohushan-Haiyuan fault. Magenta rectangles outline the three creep sections along the fault. Dotted rectangles show the locations of cross-fault profiles, which are shown below. Black dots show the median rates of InSAR points (light blue dots), their standard deviation of all the pixels (gray dots) within a 1.5-km-wide bin along the profile. The red lines in the right-hand panels represent linear fitting, and the estimated creep rate values are given; pink shading show the 95% confidence level of the linear fitting.

recovered along the fault above a depth of ~ 10 km, whereas poorer resolutions are found below a depth of ~ 10 km (Figure S10).

5. Shallow Creep and Fault Coupling Results

5.1. Fault Creep From Restored LOS Data

Figure S11 shows an average creep rate result along the Laohushan-Haiyuan fault; cross-fault profiles are within ~ 50 – 100 kilometers width and are the same as the GPS velocity profiles in Section 4.1. The results highlight that at least two sections of the Laohushan-Haiyuan fault are creeping aseismically, but the distribution of creep along the fault is not clear. Text S4 presents a detailed analysis.

On the basis of the above, Figure 5b shows a higher spatial resolution creep rate estimated from the restored InSAR LOS, which highlights four main features: (1) a ~ 30 km-long shallow creep section ($\sim 103.65^\circ\text{E}$ – 103.95°E) at the eastern end of the Laohushan fault with a rate of ~ 2 – 4 mm/a, which is consistent with velocity profile modeling results (Figure S11); (2) significant velocity offsets of up to ~ 7 mm/a across the junction ($\sim 104^\circ\text{E}$) of the Laohushan fault and western Haiyuan fault. These offsets are probably related to subsidence occurring within the Jingtai pull-apart basin, and are thus defined as outliers (Figure 5a); (3) ~ 10 km-long velocity offsets of ~ 3 – 5 mm/a across the western Haiyuan fault ($\sim 104.2^\circ\text{E}$ – 104.3°E); and (4) 43 km-long velocity offsets of ~ 1 – 3 mm/a across the eastern Haiyuan fault ($\sim 105.3^\circ\text{E}$ – 105.7°E), which we also interpret as shallow creep.

In short, our results confirm the pre-identified creep section on the Laohushan fault. Moreover, we identified two additional creep sections along the Haiyuan fault, with creep rates ranging from 1 to 5 mm/a.

5.2. Interseismic Fault Coupling From the Elastic Block Model

Block modeling results of fault slip rate and fault coupling are shown in Figures 5b and 5d, and Figure S12. Block internal strain rates and geodetic data residuals are shown in Figure S8 and S13, respectively. The Haiyuan fault system is dominated by left-lateral strike-slip motion estimated at 4–5 mm/a and decreasing eastwards. Fault normal (shortening) slip rates were estimated at 0–0.5 mm/a, consistent with those derived from cross-fault GPS velocity profiles (Figure S6).

The fault coupling results reveal a highly heterogeneous locking distribution along the Laohushan-Haiyuan fault, with four highly locked sections separated by mildly coupled or creeping segments (Figure 5d). From west to east, the asperity on the Laohushan fault has a width of at least 50 km and locking depth of approximately 20 km. The HYW asperity is locked to ~ 15 km and extends ~ 40 km laterally. The HYM asperity is more superficial, with a locking depth of less than 10 km but extending ~ 70 km along the fault strike. Finally, the HYE asperity presents a strong coupling patch between 5 and 25 km depth, and extends laterally for ~ 40 km. These three mildly locked segments overlap the creeping sections obtained from direct analysis of the restored InSAR data, although the creep rates do not show complete correspondence (Figure 5b).

6. Discussion

6.1. Uncertainties in Creep Rate Estimation

The uncertainty in creep rate estimation originates from several aspects. The first is the low signal-to-noise ratio of the restored LOS data. As detailed in Section 4.1 and Text S3, we tested multiple choices of small boxes with different widths and lengths. Despite results of all profile choices showing a similar overall along-strike pattern (Figure S7), short profiles (e.g., profile lengths of 1 km on each side of the fault) include fewer data and suffer from low signal-to-noise ratios, while long profiles (e.g., profile length of 4–5 km on each side of the fault) might overestimate the creep rate and its lateral extent. The preferred scheme of this study maintained a balance between the signal-to-noise ratio and creep rate estimation bias.

The second factor lies in the short-wavelength vertical deformation signal in the restored LOS data. The transpressional step-over near $\sim 105.7^\circ\text{E}$ (HYE creep segment) and the change in fault strike near 104.3°E (HYW creep segment) imply uplift motion, and/or a topographic effect (relief of 1–2 km across the creep

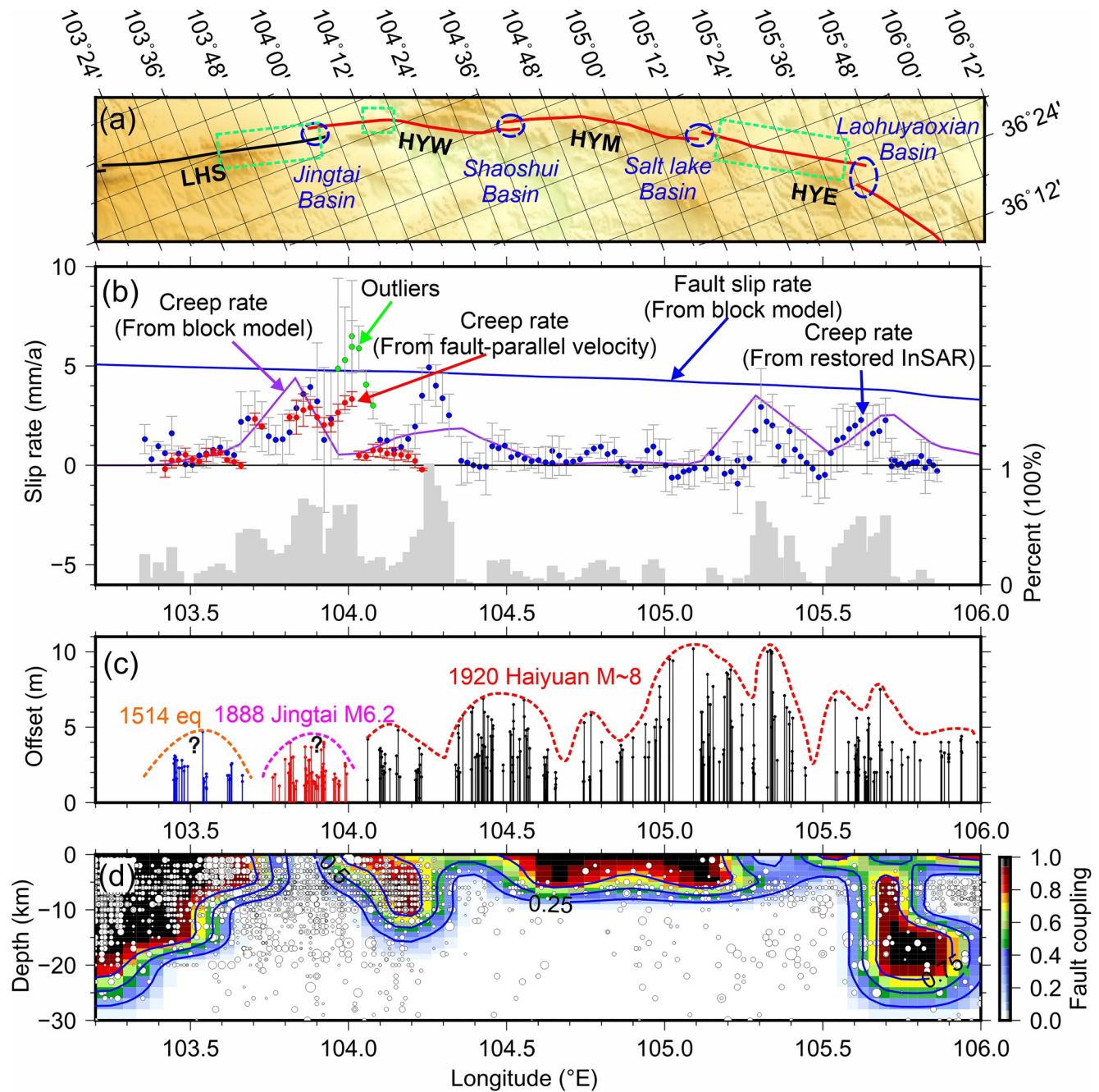


Figure 5. (a) Tectonic map across the Laohushan-Haiyuan fault. Blue ellipses outline the pull-apart basins along the fault. Green rectangles outline the three creep sections along the fault. (b) Creep rate along the Haiyuan fault. Blue dots represent creep rates calculated from the restored Interferometric Synthetic Aperture Radar (InSAR) line-of-sight (LOS) map. Red dots show creep rates estimated from the decomposed fault-parallel velocity map. Green dots indicate creep rates that are probably related to subsidence occurring within the Jingtai pull-apart basin, and thus are defined as outliers. Error bars represent 1σ uncertainties. The blue and purple lines correspond to the block model-predicted fault slip rate and fault creep rate respectively. The gray histogram shows the creep rates as a percentage of the fault slip rates. (c) Black (Q. Deng et al., 1986; Ren et al., 2016), red, and blue (Chen et al., 2018) vertical lines represent coseismic offsets across the Laohushan-Haiyuan fault induced by the 1920, 1888, and 1514 earthquakes, respectively. Question marks indicate the speculative nature of the estimates; that is, the offsets most likely relate to these paleoearthquakes but this cannot be conclusively verified (see Chen et al., [2018] for details). Dotted lines indicate the approximate displacement pattern. (d) Fault coupling along the Laohushan-Haiyuan fault. White dots indicate microseismicity ($M \geq 2$) from 1965 to 2020 (<http://data.earthquake.cn/>). Blue lines show fault coupling contours.

segments) might be present in the restored LOS map. We show a comparison between the observed and restored LOS across these two fault segments in Figure S14. The results show that, to the first order, vertical deformation (potentially including the topographic effect) was removed from the restored LOS. Figure 5b shows creep rate estimates along the Laohushan fault using both the restored LOS and the fault-parallel velocity (see Section 6.2); the two estimates are consistent. Furthermore, we show the creep rate results using both the observed LOS and restored LOS in Figure S15, in which, overall, creep rates are overestimated by using the observed LOS. The above results imply that the remove-filter-restore method could reduce the impact of short-wavelength vertical deformation to some extent. Nevertheless, short-wavelength or localized vertical deformation that has not been effectively removed could still cause overestimation of the creep rate and its lateral extent.

The third fact comes from the assumption that the restored InSAR data are purely related to the fault-parallel motion; that is, we ignored fault-normal motion. Both fault-normal components of GPS velocity and block modeling show minor shortening rates ($\sim 0\text{--}0.5$ mm/a) across the Laohushan-Haiyuan fault. In extreme cases, that is, the shortening component is completely transformed into fault vertical motion, its contribution to LOS does not exceed 0.45 mm/a, which is within the uncertainty of the InSAR data. A further related issue is the assumption of a vertical fault. Changes in fault dip along-strike are expected, as indicated by mountains to the north and south of the fault along its length. With reference to previous studies (e.g., Daout et al., 2016; Jolivet et al., 2012) and considering the minor shortening motion across the fault, we adopted a simple vertical geometry for the Laohushan-Haiyuan fault.

In summary, the above mentioned factors could either alone or in combination cause uncertainties in estimating the creep rate and creep lateral extent. Despite attempts to minimize the influence of the above factors to the degree possible, the creep characteristics of the Laohushan-Haiyuan fault cannot be completely determined without sufficient observations and verification. Continuous observations from ascending and descending InSAR will provide a database to better constrain the creep rate and lateral extent of creep segments.

6.2. New Insight Into the Laohushan Fault Creep Rate

The Laohushan creep segment has been intensively studied using InSAR observations (Cavalié et al., 2008; Daout et al., 2016; Jolivet et al., 2012, 2013). Cavalié et al. (2008) reported shallow creep along the Laohushan fault using European Remote Sensing (ERS) SAR data spanning 1993–1998. Their results show a fault slip rate of 5 mm/a beneath 15 km depth, and an average creep rate of 11 mm/a between 2 and 7 km depth. Subsequently, Jolivet et al. (2012, 2013) used Envisat SAR data (2003–2009 period) to show that the Laohushan fault creeps at a mean rate of 5 ± 1 mm/a (maximum rate of 8 ± 2 mm/a) with creep taking place between 5 and 15 km depth and extending 35 km laterally. More recently, Daout et al. (2016) obtained similar results by processing Envisat SAR data spanning the 2001–2011 period; they found a fault loading rate of 5.6 mm/a and a creep rate of 4.6 mm/a between 0.5 and 24 km depth. The limitation of these previous works is that only descending observations were used, in which eastward motion and potential vertical deformation both contribute to the apparent velocity offset across the creep section.

Since we have both descending and ascending SAR observations across the Laohushan fault (Figure 1 and S16), we were able to decompose the InSAR velocity field into fault-parallel and vertical components. We did this by first transforming the two images into the same reference frame and then resampling the LOS velocities on a 100×100 m grid. For each pixel where information from both ascending and descending geometries were available, we inverted for the fault-parallel and vertical components of the velocity using the method described by Wright et al. (2004). The fault-parallel component (Figure 6a) clearly shows creep as a velocity discontinuity on the above determined creep section ($\sim 103.65^\circ\text{E}\text{--}103.95^\circ\text{E}$). Fault-parallel components of GPS sites are consistent at the ~ 1.0 mm/a level with the decomposed fault-parallel component (Figure S17), implying that the decomposition results are credible in spite of fluctuations in the velocity field that might reflect atmospheric residuals. The other apparent feature is the uplift motion ($\sim 1\text{--}2$ mm/a; Figure 6b) across the creep section, which is consistent with and within the error range of leveling observations (Figure S17). The uplift motion is consistent with the tectonic background of compression and shortening in northeastern Tibet.

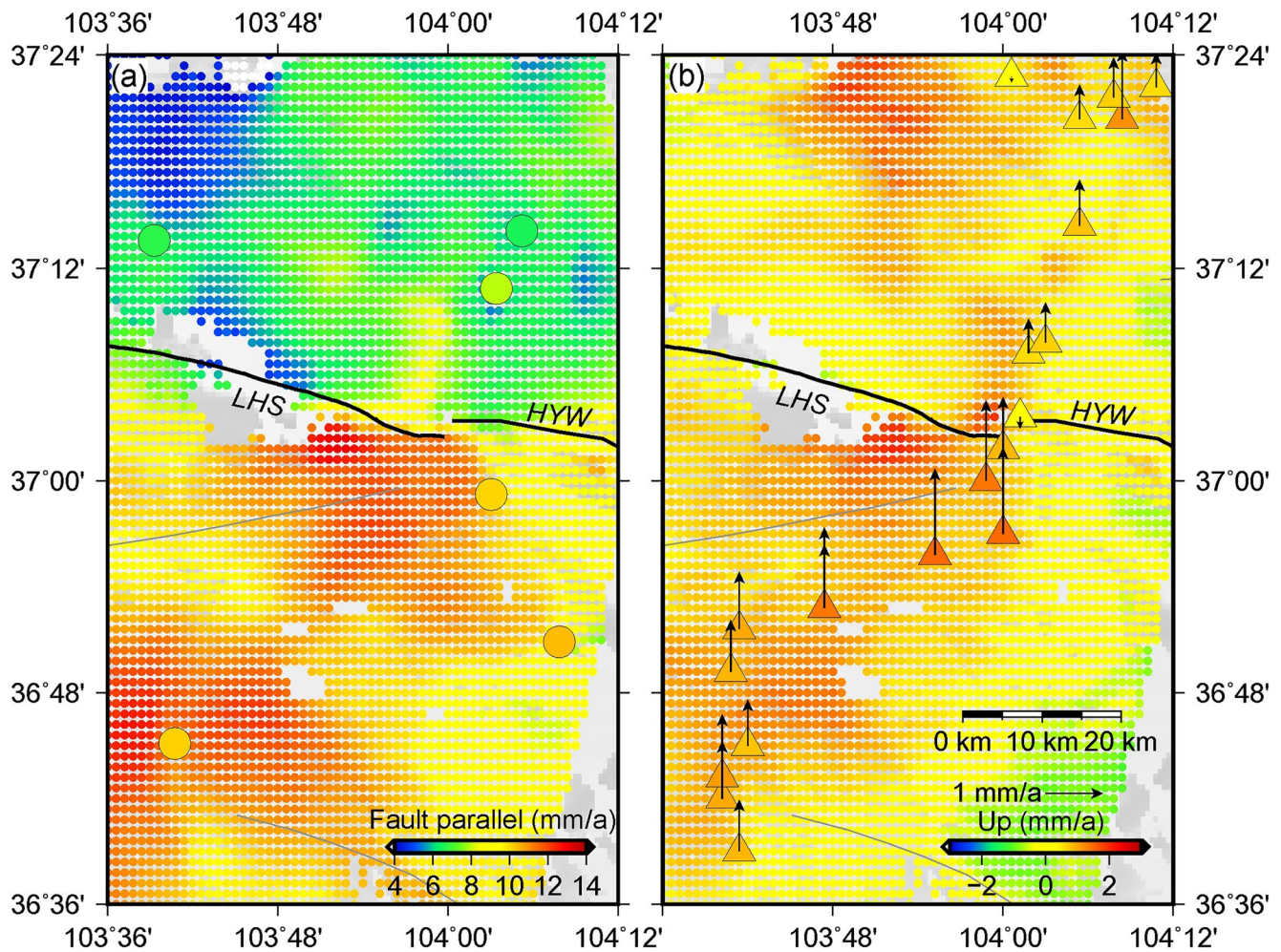


Figure 6. (a) Fault parallel and (b) vertical components of the velocity from the decomposition of descending and ascending Interferometric Synthetic Aperture Radar (InSAR) data across the Laohushan fault. Circle colors represent fault parallel components of Global Positioning System (GPS) sites; triangle colors represent leveling results (i.e., vertical rates).

Our results reveal a fault slip rate of ~ 4.8 mm/a with a smaller average creep rate of 2.5 ± 0.4 mm/a along a ~ 30 km segment, with creep encompassing almost the whole seismogenic zone (0–20 km; Figures 5b and 5d). The creep rate is the average of those results derived from the restored LOS and the fault-parallel velocity. As both InSAR and GPS data have limited resolutions at depths of >15 km (Figures S9 and S10), we do not interpret the creeping depth differences but instead focus on the creep rate and its lateral extent along strike. We attribute the discrepancies in our results with respect to previous studies to the different methods used; for example, the cross-fault velocity profile in Cavalieri et al. (2008) extends to 100 km and 3D elastic modeling was used in Jolivet et al. (2012). We also emphasize that the vertical deformation mapped into the observed InSAR LOS displacements results in creep rate discrepancies. Direct evidence is that the average creep rate was estimated to be 4.8 ± 0.4 mm/a using the observed LOS data (Figure S15), overlapping with that of previous studies. Not accounting for vertical motion could overestimate the creep rate by $\sim 50\%$.

Here, our refined surface creep rate is consistent with the 2.25 ± 2.24 mm/a creep rate (between 4 and 8 km depth) derived from repeat earthquakes on the Laohushan fault (Y. Deng et al., 2020), although at different depths. The available results provide limited information of the deformation at deeper depth of the fault, but the above two results imply slip deficit in the shallow portion of the Laohushan fault, and thus the possibility of brittle rupture.

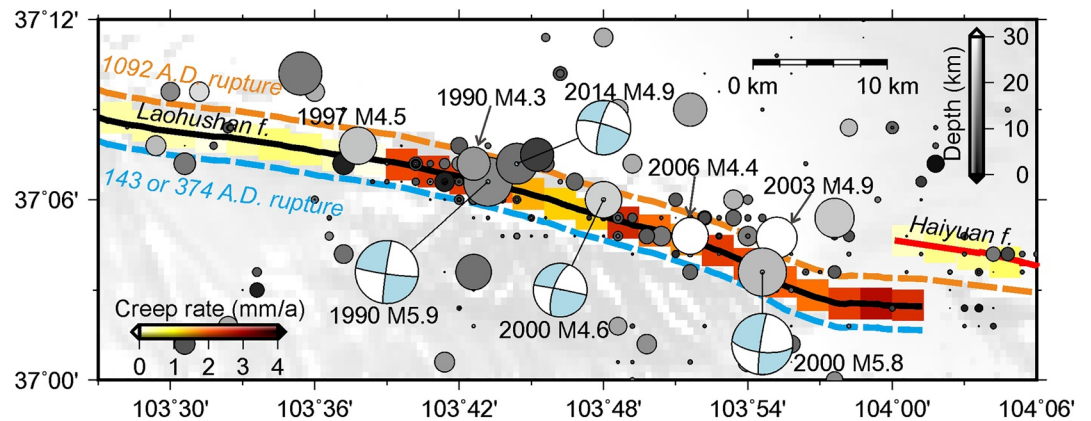


Figure 7. Creep rates and earthquakes along the Laohushan fault. Background colors represent the proposed creep rates. The bold black line represent the Laohushan fault. Dotted lines indicate the ruptures of historical earthquakes, with positions shifted for clarity (Liu-Zeng et al., 2007). The earthquake catalog and focal mechanisms are from the China Earthquake Administration (<http://data.earthquake.cn/>).

6.3. Creep Mechanism Along the Laohushan Fault

Two mechanisms have been proposed to explain the Laohushan creep. Jolivet et al. (2013) proposed that the fault creep witnesses a velocity strengthening regime at shallow depths, persistent though time. As a consequence, they suggested that the observed creep segment may act as a persistent barrier to earthquake propagation. Chen et al. (2018) proposed that the Laohushan fault creep might be afterslip following the 2000 Jingtai Mw 5.5 earthquake and/or a response to the 1920 M~8 Haiyuan earthquake, and would thus reflect transient behavior.

Our results show that aseismic slip accounts only for ~44%–60% of the tectonic loading rate (Figure 5b). The remaining slip deficit might be released partially by the frequent ruptures of small asperities indicated by a high density of small earthquakes (Figure 7), with occasional moderate-size events such as the 1990 Mw 5.7 earthquake and 2000 Mw 5.5 earthquake. Creeping regions of faults might encompass locked patches sprinkled along the overall creeping fault plane, still allowing for earthquake nucleation and rupture propagation (Wei et al., 2013). Even for stable creeping areas, laboratory experiments have shown that earthquakes may occur solely owing to a high stressing rate (McLaskey & Kilgore, 2013); besides, numerical simulations show that earthquakes can propagate along-strike for a considerable distance into a creeping section of the fault (e.g., Noda & Lapusta, 2013). In this case, a nearby rapid stress increment could convert a creeping patch into an unstable patch, allowing rupture propagation (Harris, 2017). Indeed, paleoearthquake investigations have identified at least two large earthquakes (similar to the 1920 M~8 Haiyuan earthquake; the first in 143 or 374 A.D. and the second in 1902 A.D.; Figure 7) that ruptured the whole Laohushan fault (Liu-Zeng et al., 2007). This suggests that, despite a long recurrence time for large earthquakes, the Laohushan creep segment has experienced seismic ruptures and hence does not act systematically as a persistent barrier as suggested by Jolivet et al. (2013).

The Laohushan creep is not likely the afterslip of the 2000 Mw 5.5 earthquake as proposed by Chen et al. (2018). An earthquake of Mw 5.5 is expected to rupture the fault plan over a few (<10 km) kilometers (Wells & Coppersmith, 1994). The 2000 Mw 5.5 earthquake occurred at the eastern end of the creep section, making it unlikely to produce afterslip extending ~20 km further west (Figure 7), although abnormally large aseismic slip following moderate earthquakes has been documented for some rare events (e.g., Villegas-Lanza et al., 2016). InSAR observations during the 1993–1998 period reveal shallow creep at a rate of ~11 mm/a (Cavalié et al., 2008), even larger than that during the 2003–2011 period (~5 mm/a; Daout et al., 2016; Jolivet et al., 2012, 2013), suggesting a decay of creep rate through time. Although these observations do not support afterslip following the 2000 Mw 5.5 earthquake, creep activated by the 1920 M~8 Haiyuan earthquake or related to the long-term afterslip of the 1920 event remain possible scenarios.

Physical and chemical processes, such as rock types, high pressure fluids, elevated pore pressures, elevated temperatures, fault geometry, or combinations of these factors, provide other possible explanations for

creep (e.g., Harris, 2017). A recent field investigation (Liu et al., 2019) found high-carbon and thick fault gouge on the creeping segment (37.066583°N, 103.900,250°E), which was suggested to allow for fault creep. However, gouge is observed elsewhere along the fault and does not always correlate with shallow creep segments. Therefore, the mechanism of the observed creep cannot be conclusively identified without further geological and geodetic observations.

6.4. Aseismic Creep and the 1920 M~8 Haiyuan Earthquake

Two additional creep sections along the 1920 M~8 Haiyuan earthquake rupture—HYW (~104.2°E–104.3°E) and HYE (~105.3°E–105.7°E)—are identified in the surface LOS map and block modeling results. Small discrepancies between the two results are due to the difficulty of highlighting short-scale localized creep signals using the block model (Figure 5b).

Figure 5c shows the coseismic surface offsets of the 1920 M~8 Haiyuan earthquake mapped by Q. Deng et al. (1986) and Ren et al. (2016). Pull-apart basins (Figure 5a) match well to sections with small magnitude surface offsets, which is expected considering their role (i.e., forming step-overs) in impeding earthquake ruptures (e.g., Lettis et al., 2002). The HYW creep section overlaps a section of lower (~3 m) surface coseismic offset. The HYE creep section has surface offsets of ~3–10 m and only partially overlaps with a small surface offset section (~105.4°E–105.6°E); surface offsets significantly decrease eastward when crossing the creep section. The limited information prevents us from further discussing the relationship between creep and earthquake rupture. Although, one possible scenario is that present-day creep contributes to a fill slip deficit still missing after the 1920 earthquake rupture and represents a kind of afterslip; in other words, it is a continuation of postseismic fault slip as suggested by Çakir et al. (2012). Alternatively, the creep might represent a persistent feature.

Afterslip is commonly observed along fault areas that exhibit aseismic slip following large earthquakes, and the fault's creep-rate should be inversely proportional to the time since the earthquake (e.g., Perfettini & Avouac, 2004). On the Haiyuan fault, afterslip lasting for ~100 years after the 1920 M~8 Haiyuan earthquake would be extremely long compared with the timescales of months to years more often observed (Savage et al., 2005). Nevertheless, abnormally long and large afterslip has been documented for a growing number of earthquakes. For instance, the 2004 Mw 6.0 Parkfield earthquake had afterslip lasting ~6–12 years (e.g., Lienkaemper & McFarland, 2017), while the 1944 Mw 7.4 earthquake along the NAF might registered afterslip for 50–70 years (e.g., Cetin et al., 2014).

6.5. Implications for Seismic Hazard

We calculated the seismic moment budget on the identified asperities. Assuming that the present-day inverted fault coupling is representative of the fault locking pattern since the 1920 M~8 Haiyuan earthquake, we calculated seismic moment accumulation rates of 2.36×10^{16} N·m/a, 1.27×10^{16} N·m/a, 9.14×10^{15} N·m/a, and 2.03×10^{16} N·m/a on the LHS, HYW, HYM, and HYE respectively. Taking the 1092 earthquake ($M > 8$; Liu-Zeng et al., 2007; Figure 7), which ruptured the whole Laohushan fault and most probably reset all of the elastic strain, as the starting date for strain accumulation, and assuming a moment magnitude of 6.0–6.5 for the 1888 earthquake, we calculated a total seismic moment of 1.56×10^{19} – 2.08×10^{19} N·m on the Laohushan fault. An equivalent single event with moment magnitude of 6.8–6.9 is required to balance the moment. Using the seismic moment accumulation rate, we calculated moment deficits of 1.25×10^{18} N·m on the HYW, 9.05×10^{17} N·m on the HYM, and 2.0×10^{18} N·m on the HYE since 1920, corresponding to earthquakes of Mw 6.0, Mw 5.9, and Mw 6.2, respectively. However, the seismic potential might be overestimated, as fault coupling might change over time (i.e., progressively relocking after large earthquakes).

The above calculation assumes asperities rupture separately; however, cascade ruptures are also possible. Specifically, the present-day slip deficit would allow the Haiyuan fault to host an earthquake with moment magnitude ranging from 5.9 to 6.3. There is clearly a discrepancy here if we consider the magnitude (M~8) of the 1920 earthquake, which might have originated from a shallow fault locking depth. If we assume those three asperities are fully locked down to 15 km, they are capable of generating earthquakes with magnitudes ranging from 7.3 (Mw) to 7.7 (Mw) every 1000 years, a value roughly consistent with the magnitude of the 1920 event. The above calculation therefore implies that the current fault locking along the Haiyuan fault

is transient on the scale of earthquake cycles, contrary to our conventional understanding that faults are locked immediately or within months after large earthquakes. Besides, a plausible inference is that the 1920 M~8 Haiyuan event, which broke multiple segments/asperities, was a rare event and not a characteristic earthquake. Indeed, paleoearthquake studies have identified moderate-size earthquakes (M~6–7) on the Haiyuan fault, and suggest that the Haiyuan fault did not always break in multi-segment rupture events before the 1920 earthquake (e.g., Liu-Zeng et al., 2015).

7. Conclusions

This study presents a dense interseismic GPS/InSAR velocity field for northeastern Tibet. Detailed comparisons among GPS, InSAR, and leveling data highlight either long-wavelength systematic errors or vertical deformation in InSAR; the latter could not be fitted by leveling and GPS vertical velocities. We thus used a filter approach to remove the long wavelength signal in the observed InSAR LOS rate map, to combine horizontal GPS with the observed InSAR data, and to obtain a continuous LOS rate map around the Laohushan-Haiyuan fault.

Geodetic data analysis shows three creeping sections along the Laohushan-Haiyuan fault. (1) A previously identified Laohushan creep segment. Both the restored LOS and the decomposed ascending and descending InSAR data indicate that vertical deformation causes the creep rate to be overestimated. Our refined results show that the Laohushan fault creeps at a rate of 2.5 ± 0.4 mm/a along a ~30 km long segment. (2) The HYW creeps at a rate of ~3–5 mm/a along a 10 km-long section. (3) The HYE creeps at ~1–3 mm/a and extends 43 km-long laterally.

The HYW and HYE creep segments are located along fault sections that ruptured during the 1920 M~8 earthquake, suggesting that the creep is (1) either the afterslip of the 1920 M~8 Haiyuan earthquake, implying heterogeneous relocking of faults after large earthquakes and creep lasting decades on some parts of the rupture; (2) or a more long-term persistent feature, suggesting that large ruptures can cross previously existing creeping segments.

Elastic block modeling of present-day fault coupling along the Laohushan-Haiyuan fault highlights highly heterogeneous slip deficit accumulation rates along strike, and implies that fault coupling might significantly evolve during the period between two large earthquakes.

Acknowledgments

The authors appreciate the detailed and constructive comments of two reviewers (Ziyadin Çakir and Teng Wang), the Editor (Paul Tregoning), and the organizers of the special section, who greatly helped to improve the quality of this work. We are grateful to all colleagues who participated in GPS station construction and measurements. Our thanks to all of the postgraduate students who engaged in the field work over the past few years. Special thanks to Chunyan Qu for her dedicated work in the field. Our gratitude to Cavalie Olivier for fruitful discussions and comments on early drafts. The current work also benefited from discussions with Dezheng Zhao and Lifeng Wang. This work is supported by the National Key Research and Development Project of China (Grant No. 2019YFC1509205) and the National Natural Science Foundation of China (Grant No. 41631073). Yanchuan Li was financially supported by the China Scholarship Council and the China Earthquake Administration. We also extend our thanks to Tornillo Scientific for language editing.

Data Availability Statement

CMONOC GPS data were provided by the National Earthquake Infrastructure Service of China Earthquake Administration. Figures were generated using the Generic Mapping Tools (GMT) software (Wessel et al., 2013). GPS velocity solutions supporting the conclusions of this study are available at <https://osf.io/8b72w/>. The InSAR LOS solution is available through Song et al. (2019).

References

- Altamimi, Z., Métivier, L., Reischung, P., Rouby, H., & Collilieux, X. (2017). ITRF2014 plate motion model. *Geophysical Journal International*, 209, 1906–1912. <https://doi.org/10.1093/gji/ggx136>
- Avouac, J. P. (2015). From geodetic imaging of seismic and aseismic fault slip to dynamic modeling of the seismic cycle. *Annual Review of Earth and Planetary Sciences*, 43, 233–271. <https://doi.org/10.1146/annurev-earth-060614-105302>
- Bilham, R., Ozener, H., Mencin, D., Dogru, A., Ergintav, S., Çakir, Z., et al. (2016). Surface creep on the North Anatolian fault at Ismetpasa, Turkey, 1944–2016. *Journal of Geophysical Research: Solid Earth*, 121, 7409–7431. <https://doi.org/10.1002/2016jb013394>
- Bürgmann, R., Schmidt, D., Nadeau, R. M., d'Alessio, M., Fielding, E., Manaker, D., et al. (2000). Earthquake potential along the northern Hayward fault, California. *Science*, 289, 1178–1182. <https://doi.org/10.1126/science.289.5482.1178>
- Çakir, Z., Akoglu, A. M., Belabbes, S., Ergintav, S., & Meghraoui, M. (2005). Creeping along the Ismetpasa section of the North Anatolian fault (Western Turkey): Rate and extent from InSAR. *Earth and Planetary Science Letters*, 238, 225–234. <https://doi.org/10.1016/j.epsl.2005.06.044>
- Çakir, Z., Ergintav, S., Ozener, H., Dogan, U., Akoglu, A. M., Meghraoui, M., & Reilinger, R. (2012). Onset of aseismic creep on major strike-slip faults. *Geology*, 40, 1115–1118. <https://doi.org/10.1130/g33522.1>
- Cavalie, O., Lasserre, C., Doin, M. P., Peltzer, G., Sun, J., Xu, X., & Shen, Z. -K. (2008). Measurement of interseismic strain across the Haiyuan fault (Gansu, China), by InSAR. *Earth and Planetary Science Letters*, 275, 246–257. <https://doi.org/10.1016/j.epsl.2008.07.057>
- Cetin, E., Çakir, Z., Meghraoui, M., Ergintav, S., & Akoglu, A. M. (2014). Extent and distribution of aseismic slip on the Ismetpaşa segment of the North Anatolian Fault (Turkey) from Persistent Scatterer InSAR. *Geochemistry, Geophysics, Geosystems*, 15, 2883–2894. <https://doi.org/10.1002/2014gc005307>

- Chaussard, E., Bürgmann, R., Fattahi, H., Johnson, C. W., Nadeau, R., Taira, T., & Johanson, I. (2015). Interseismic coupling and refined earthquake potential on the Hayward-Calaveras fault zone. *Journal of Geophysical Research: Solid Earth*, *120*(12), 8570–8590. <https://doi.org/10.1002/2015jb012230>
- Chen, T., Liu-Zeng, J., Shao, Y., Zhang, P., Oskin, M. E., Lei, Q., & Li, Z. (2018). Geomorphic offsets along the creeping Laohu Shan section of the Haiyuan fault, northern Tibetan Plateau. *Geosphere*, *14*, 1165–1186. <https://doi.org/10.1130/ges01561.1>
- Daout, S., Jolivet, R., Lasserre, C., Doin, M. P., Barbot, S., Tapponnier, P., et al. (2016). Long-strike variations of the partitioning of convergence across the Haiyuan fault system detected by InSAR. *Geophysical Journal International*, *205*, 536–547. <https://doi.org/10.1093/gji/ggw028>
- Deng, Q., Chen, S., Song, F., Zhu, S., Wang, Y., Zhang, W., et al. (1986). Variations in the geometry and amount of slip on the Haiyuan (Nanxihaushan) fault zone, China, and the surface rupture of the 1920 Haiyuan earthquake. *Earthquake Source Mechanics, Geophys. Monograph Series*, *37*, 169–182.
- Deng, Y., Peng, Z., & Liu-Zeng, J. (2020). Systematic search for repeating earthquakes along the Haiyuan fault system in northeastern Tibet. *Journal of Geophysical Research: Solid Earth*, *125*, e2020JB019583. <https://doi.org/10.1029/2020jb019583>
- Diao, F., Wang, R., Wang, Y., Xiong, X., & Walter, T. R. (2018). Fault behavior and lower crustal rheology inferred from the first seven years of postseismic GPS data after the 2008 Wenchuan earthquake. *Earth and Planetary Science Letters*, *495*, 202–212. <https://doi.org/10.1016/j.epsl.2018.05.020>
- Gan, W., Zhang, P., Shen, Z.-K., Niu, Z., Wang, M., Wan, Y., et al. (2007). Present-day crustal motion within the Tibetan Plateau inferred from GPS measurements. *Journal of Geophysical Research*, *112*, B08416. <https://doi.org/10.1029/2005jb004120>
- Gaudemer, Y., Tapponnier, P., Meyer, B., Peltzer, G., Guo, S., Chen, Z., et al. (1995). Partitioning of crustal slip between linked, active faults in the eastern Qilian Shan, and evidence for a major seismic gap, the ‘Tianzhu gap’, on the western Haiyuan Fault, Gansu (China). *Geophysical Journal International*, *120*, 599–645. <https://doi.org/10.1111/j.1365-246x.1995.tb01842.x>
- Hao, M., Wang, Q., Shen, Z., Cui, D., Ji, L., Li, Y., & Qin, S. (2014). Present day crustal vertical movement inferred from precise leveling data in eastern margin of Tibetan Plateau. *Tectonophysics*, *632*, 281–292. <https://doi.org/10.1016/j.tecto.2014.06.016>
- Harris, R. A. (2017). Large earthquakes and creeping faults. *Reviews of Geophysics*, *55*, 169–198. <https://doi.org/10.1002/2016rg000539>
- Herring, T. A., King, R. W., Floyd, M. A., & McCluskey, S. C. (2016). Introduction to GAMIT/GLOBK, Release 10.6. Massachusetts Institute of Technology.
- Jolivet, R., Lasserre, C., Doin, M. P., Guillaso, S., Peltzer, G., Dailu, R., et al. (2012). Shallow creep on the Haiyuan fault (Gansu, China) revealed by SAR interferometry. *Journal of Geophysical Research*, *117*, B06401. <https://doi.org/10.1029/2011jb008732>
- Jolivet, R., Lasserre, C., Doin, M. P., Peltzer, G., Avouac, J. P., Sun, J., & Dailu, R. (2013). Spatio-temporal evolution of aseismic slip along the Haiyuan fault, China: Implications for fault frictional properties. *Earth and Planetary Science Letters*, *377*, 23–33. <https://doi.org/10.1016/j.epsl.2013.07.020>
- Kreemer, C., Blewitt, G., & Klein, E. C. (2014). A geodetic plate motion and Global Strain Rate Model. *Geochemistry, Geophysics, Geosystems*, *15*, 3849–3889. <https://doi.org/10.1002/2014gc005407>
- Lettis, W., Bachhuber, J., Witter, R., Brankman, C., Randolph, C. E., Barka, A., et al. (2002). Influence of releasing step-overs on surface fault rupture and fault segmentation: Examples from the 17 August 1999 Izmit Earthquake on the North Anatolian Fault, Turkey. *Bulletin of the Seismological Society of America*, *92*, 19–42. <https://doi.org/10.1785/0120000808>
- Li, Y., Liu, M., Wang, Q., & Cui, D. (2018). Present-day crustal deformation and strain transfer in northeastern Tibetan Plateau. *Earth and Planetary Science Letters*, *487*, 79–189. <https://doi.org/10.1016/j.epsl.2018.01.024>
- Li, Y., Shan, X., Qu, C., Liu, Y., & Han, N. (2018). Crustal deformation of the Altyn Tagh fault based on GPS. *Journal of Geophysical Research: Solid Earth*, *123*, 10309–10322. <https://doi.org/10.1029/2018jb015814>
- Li, Y., Shan, X., Qu, C., & Wang, Z. (2016). Fault locking and slip rate deficit of the Haiyuan-Liupanshan fault zone in the northeastern margin of the Tibetan Plateau. *Journal of Geodesy*, *102*, 47–57. <https://doi.org/10.1016/j.jog.2016.07.005>
- Li, Y., Shan, X., Qu, C., Zhang, Y., Song, X., Jiang, Y., et al. (2017). Elastic block and strain modeling of GPS data around the Haiyuan-Liupanshan fault, northeastern Tibetan Plateau. *Journal of Asian Earth Sciences*, *150*, 87–97. <https://doi.org/10.1016/j.jseas.2017.10.010>
- Liang, S., Gan, W., Shen, C., Xiao, G., Liu, J., Chen, W., et al. (2013). Three-dimensional velocity field of present-day crustal motion of the Tibetan Plateau derived from GPS measurements. *Journal of Geophysical Research: Solid Earth*, *118*, 5722–5732. <https://doi.org/10.1002/2013jb010503>
- Lienkaemper, J. J., & McFarland, F. S. (2017). Long-term afterslip of the 2004 M 6.0 Parkfield, California, Earthquake—Implications for forecasting amount and duration of afterslip on other major creeping faults. *Bulletin of the Seismological Society of America*, *107*, 1082–1093. <https://doi.org/10.1785/0120160321>
- Lienkaemper, J. J., McFarland, F. S., Simpson, R. W., & Caskey, S. J. (2014). Using surface creep rate to infer fraction locked for sections of the San Andreas Fault system in northern California from alignment array and GPS data. *Bulletin of the Seismological Society of America*, *104*, 3094–3114. <https://doi.org/10.1785/0120140117>
- Liu, Y., Liu, C., Zhang, Z., Liu, K., Ren, Z., Zhang, H., et al. (2019). Rock magnetic studies of fault rocks from the Laohushan segment of the Haiyuan fault zone and its tectonic implications. *Chinese Journal of Geophysics*, *63*, 2311–2328.
- Liu-Zeng, J., Klinger, Y., Xu, X., Lasserre, C., Chen, G., Chen, W., et al. (2007). Millennial recurrence of large earthquakes on the Haiyuan fault near Songshan, Gansu Province, China. *Bulletin of the Seismological Society of America*, *97*, 14–34. <https://doi.org/10.1785/0120050118>
- Liu-Zeng, J., Shao, Y., Klinger, Y., Xie, K., Yuan, D., & Lei, Z. (2015). Variability in magnitude of paleoearthquakes revealed by trenching and historical records, along the Haiyuan Fault, China. *Journal of Geophysical Research: Solid Earth*, *120*, 8304–8333.
- McCaffrey, R. (2009). Time-dependent inversion of three-component continuous GPS for steady and transient sources in northern Cascadia. *Geophysical Research Letters*, *36*, L07304. <https://doi.org/10.1029/2008gl036784>
- McLaskey, G. C., & Kilgore, B. D. (2013). Foreshocks during the nucleation of stick-slip instability. *Journal of Geophysical Research: Solid Earth*, *118*, 2982–2997. <https://doi.org/10.1002/jgrb.50232>
- Nocquet, J. M. (2017). PYACS: A set of Python tools for GPS analysis and tectonic modeling. Colloque G2 2017, geodesy-rheology.
- Noda, H., & Lapusta, N. (2013). Stable creeping fault segments can become destructive as a result of dynamic weakening. *Nature*, *493*, 518–521. <https://doi.org/10.1038/nature11703>
- Perfettini, H., & Avouac, J.-P. (2004). Postseismic relaxation driven by brittle creep: A possible mechanism to reconcile geodetic measurements and the decay rate of aftershocks, application to the Chi-Chi earthquake, Taiwan. *Journal of Geophysical Research*, *109*, B02304. <https://doi.org/10.1029/2003jb002488>
- Reid, H. F. (1910). On mass movements in tectonic earthquakes and the depth of the focus. *Beitragen Geophysics*, *10*, 318–351.
- Ren, Z., Zhang, Z., Chen, T., Yan, S., Yin, J., Zhang, P., et al. (2016). Clustering of offsets on the Haiyuan fault and their relationship to paleoearthquakes. *Geological Society of America Bulletin*, *128*, 3–18. <https://doi.org/10.1130/B31155.1>

- Rosen, P. A., Hensley, S., Peltzer, G., & Simons, M. (2004). Updated repeat orbit interferometry package released. *Eos, Transactions American Geophysical Union*, 85, 47. <https://doi.org/10.1029/2004eo050004>
- Sandwell, D. T., & Wessel, P. (2016). Interpolation of 2-D vector data using constraints from elasticity. *Geophysical Research Letters*, 43, 10703–10709. <https://doi.org/10.1002/2016gl070340>
- Savage, J. C., Svarc, J. L., & Yu, S.-B. (2005). Postseismic relaxation and transient creep. *Journal of Geophysical Research*, 110, B11402. <https://doi.org/10.1029/2005jb003687>
- Song, X., Jiang, Y., Shan, X., Gong, W., & Qu, C. (2019). A fine velocity and strain rate field of present-day crustal motion of the northeastern Tibetan Plateau inverted jointly by InSAR and GPS. *Remote Sens*, 11, 435. <https://doi.org/10.3390/rs11040435>
- Villegas-Lanza, J., Nocquet, J., Rolandone, F., Vallée, M., Tavera, H., Bondoux, F., et al. (2016). A mixed seismic-aseismic stress release episode in the Andean subduction zone. *Nature Geoscience*, 9(2), 150–154. <https://doi.org/10.1038/ngeo2620>
- Wei, M., Kaneko, Y., Liu, Y., & McGuire, J. J. (2013). Episodic fault creep events in California controlled by shallow frictional heterogeneity. *Nature Geoscience*, 6, 566–570. <https://doi.org/10.1038/ngeo1835>
- Wei, M., Sandwell, D., & Smith-Konter, B. (2010). Optimal combination of InSAR and GPS for measuring interseismic crustal deformation. *Advances in Space Research*, 46, 236–249. <https://doi.org/10.1016/j.asr.2010.03.013>
- Wells, D. L., & Coppersmith, K. J. (1994). New empirical relationships among magnitude, rupture length, rupture width, rupture area, and surface displacement. *Bulletin of the Seismological Society of America*, 84, 974–1002.
- Wessel, P., Smith, W. H., Scharroo, R., Luis, J., & Wobbe, F. (2013). Generic mapping tools: Improved version released. *Eos, Transactions American Geophysical Union*, 94, 409–410. <https://doi.org/10.1002/2013eo450001>
- Wright, T. J., Parsons, B. E., & Lu, Z. (2004). Toward mapping surface deformation in three dimensions using InSAR. *Geophysical Research Letters*, 31, L01607. <https://doi.org/10.1029/2003gl018827>